Chapter 6

LOW FREQUENCY ELECTROOPTIC RESPONSE IN SOME HIGHLY POLAR COMPOUNDS

6.1 Introduction

In Chapters 3 and 4 we have discussed experimental results which describe the effect of an AC electric field (with a frequency of a few kHz) on the orientational order in a strongly polar medium and its effect on the phase trahsition temperatures. In the previous chapter we have shown that there is sufficient evidence for a polar short range order in the compound studied which gives rise to some unusual results. Even before conducting these experiments we had taken up electrooptic studies in the nematic phase of a few compounds with large positive dielectric anisotropy to look for a signal which could result from the response of polar domains to the applied electric field.

We specifically looked for such a signal in the compound 5CT which was already known to have both partial bilayer and monolayer short range order (the chemical names of the compounds are given on the next page). Xray studies on 5CT [86] show that the monolayer short range order is prevalent at temperatures below $\sim 150^{o}C$ while the bilayer short range order is favoured at higher temperatures. We also studied a structurally similar compound *viz.* ROCP7334 and 8OCB. Xray studies on 80CB [87] show that it has only a partial bilayer short range order in the nematic phase. At low frequencies ($\sim$ 256 Hz) of a sufficiently high applied square wave voltage an electrooptic response was seen in these compounds, which is at twice the frequency of the applied voltage. Higher even harmonic optical responses were also observed. The neighbouring odd harmonic components of the optical signal are much smaller than the even harmonic signals (by an order of magnitude). The onset of the electrooptic response is found to coincide with the current getting limited in the sample. This indicates that there is an electrolytic process taking place in the sample cell which is important to the onset of the electrooptic response. We discuss the possible origins of the optical response to arise either from an electrohydrodynamic instability or a coupling of the flexoelectricity (polarisation induced by the distortion of the director [88]) with a field gradient formed in the sample due to the electrolytic effect. Polar short range order does not appear to be important to the observed results.

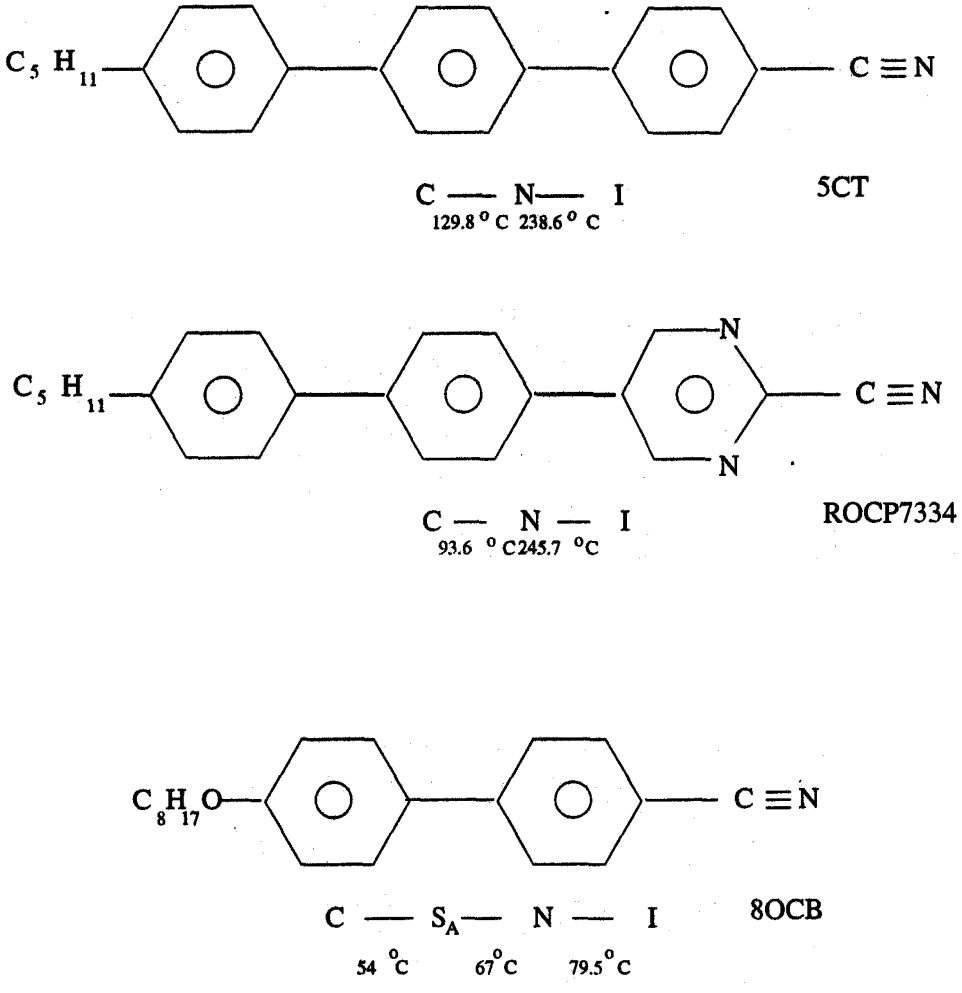

Figure 6.1: Chemical structures and transition temperatures of the compounds used in the experiments described in this chapter.

6.2 Experimental

6.2.1 High field Electrooptic Response

We have conducted the experiments on the following compounds: octyloxycyano biphenyl (8OCB, $\epsilon_a \simeq 8$ at T = 70°C), pentyl cyanoterphenyl (5CT, $\epsilon_a \simeq 12.5$ at T = 130°C) and butylphenyl cyanophenyl-pyrimidine (ROCP7334, $\epsilon_a \simeq 22$ at T = 100°C). The chemical structures and transition temperatures of the compounds are shown in Figure 6.1. The samples were obtained from Roche and were used without further purification.

The samples were taken between two transparent ITO coated glass plates which were pretreated with ODSE for homeotropic alignment of the director. 23 μm mylar spacers were used to control the thickness of the cell. The thickness of the cell was measured using channeled spectrum as described in Chapter 2. The typical active area of the cell was $\sim 1\ cm^2$.

The cell is kept in a Mettler hot stage which itself is placed between crossed polarisers on the stage of a polarising microscope. The sample is illuminated with a He-Ne laser beam ($\lambda = 0.633\ \mu m$) along the director of the homeotropically aligned sample (Figure 6.2). The

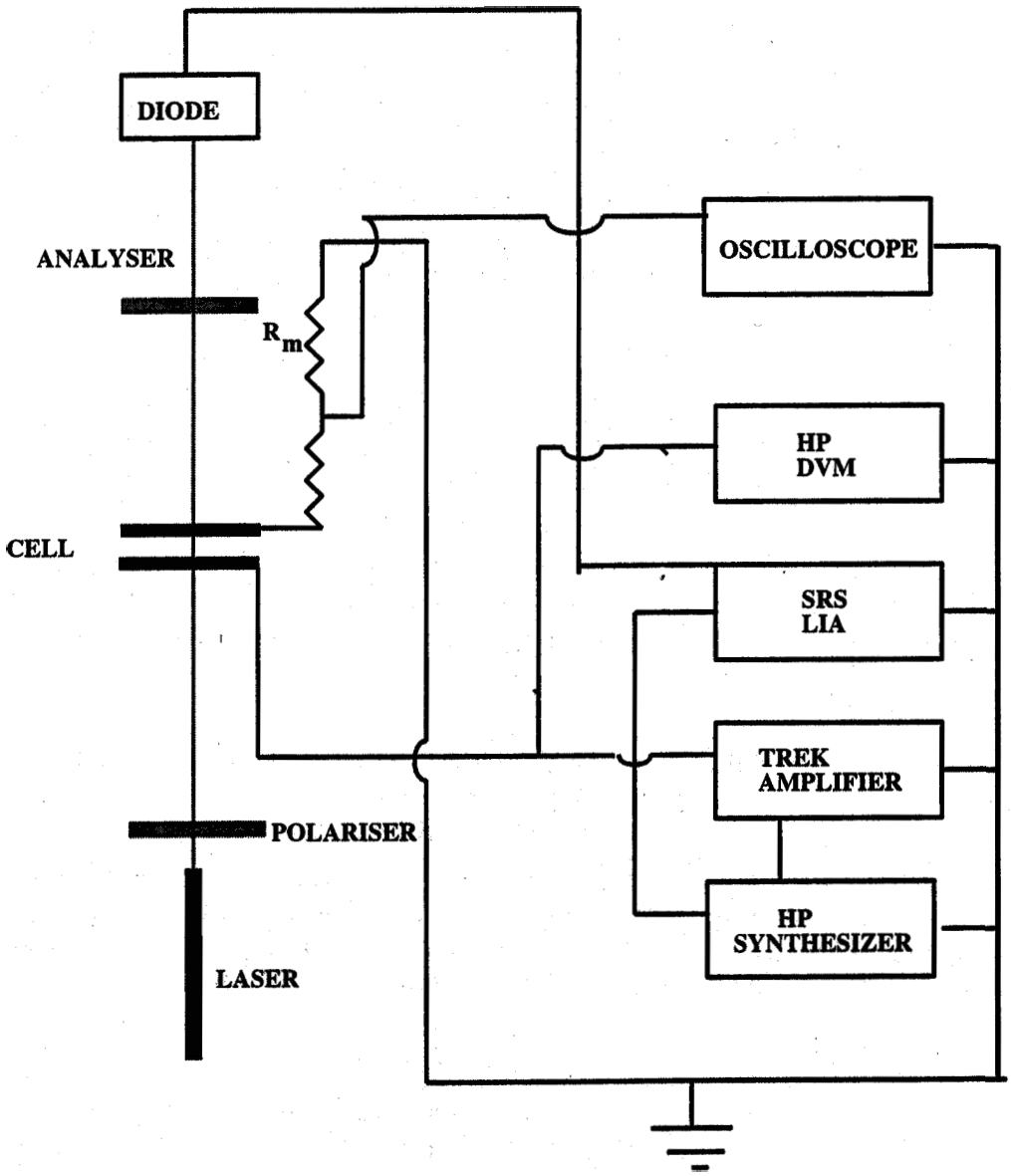

Figure 6.2: Schematic diagram of the experimental setup used to conduct the electrooptic measurements.

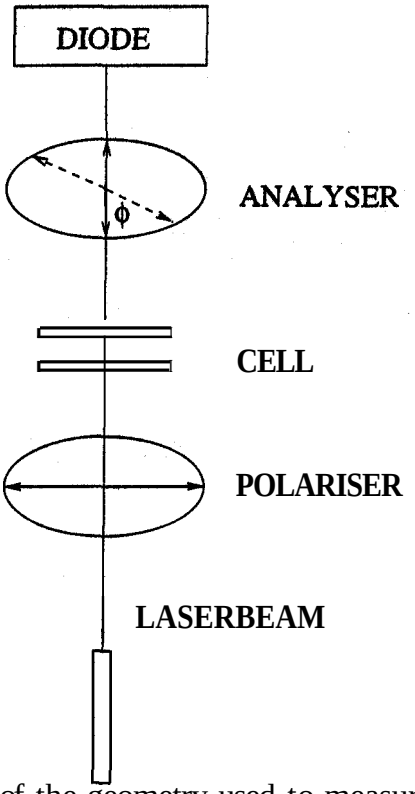

Figure 6.3: Schematic diagram of the geometry used to measure I_o. The solid arrows indicate the vibration direction of the analyser and polariser in the crossed position. The dashed arrow indicates the vibration direction of the analyser at an angle ϕ with respect to the crossed polariser position.

optical response is monitored using an OSD-5 CENTRONICS photodiode. The DC component of the optical signal is measured using a Keithley multimeter (model 173) and the AC component is measured using a lock-in-amplifier (LIA, model SRS 830).

To measure the absolute intensity of the optical response we need to know the intensity of the incident light (I_o). We measure I_o with the homeotropically aligned sample positioned in the heater. The DC optical intensity (I_{DC}) is measured as a function of the analyser setting around the position crossed with respect to the polariser (Figure 6.3). I_{DC} is assumed to be of the form

$$I_{DC} = I_{back} + I_o \sin^2 \phi \tag{6.1}$$

where ϕ is the angle made by the vibration direction of the analyser with respect to the crossed polarisers position. I_{back} is the background contribution due to the dark current of the diode. Figure 6.4 shows the typical variation of I_{DC} as a function of analyser settings. Figure 6.5 shows the variation of the DC optical signal as a function of $\sin^2 \phi$. I_o is obtained by fitting a straight line to Equation 6.1. The AC optical response is then $\frac{I_{AC}}{I_o}$, where I_{AC} is the optical signal measured by the LIA.

A square wave voltage is derived from an HP synthesizer (model 3326A) and is amplified by a Trek amplifier (model 301B). The amplified voltage is fed to the sample cell which is in series with two resistors the sum of which =1.1 kΩ (Figure 6.2). The amplitude of the amplified voltage is measured using an HP multimeter (model 3458A). The HP synthesizer output is also fed to the external reference terminal of the LIA. The electrical current flowing through the sample is simultaneously monitored using an oscilloscope by measuring the voltage drop across the series resistor (R_m). Figure 6.6 shows a typical variation of the voltage drop across R_m as

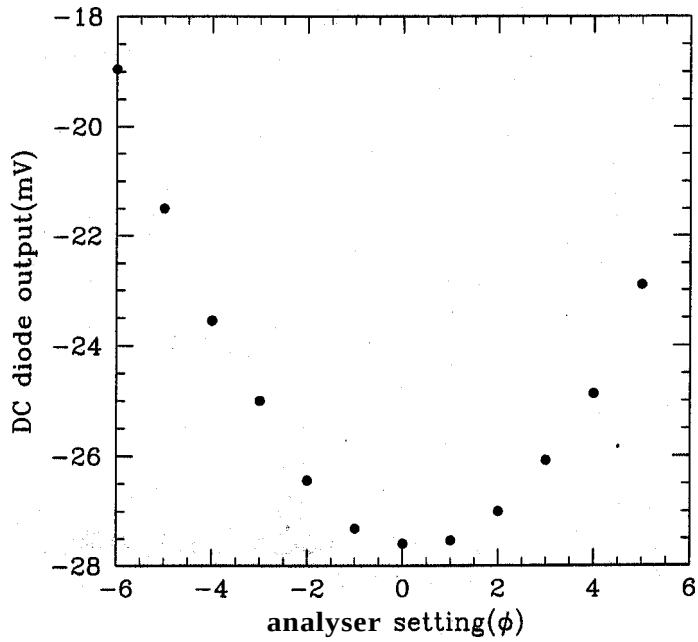

Figure 6.4: Typical variation of the transmitted light intensity as measured by the photodiode as a function of analyser settings.

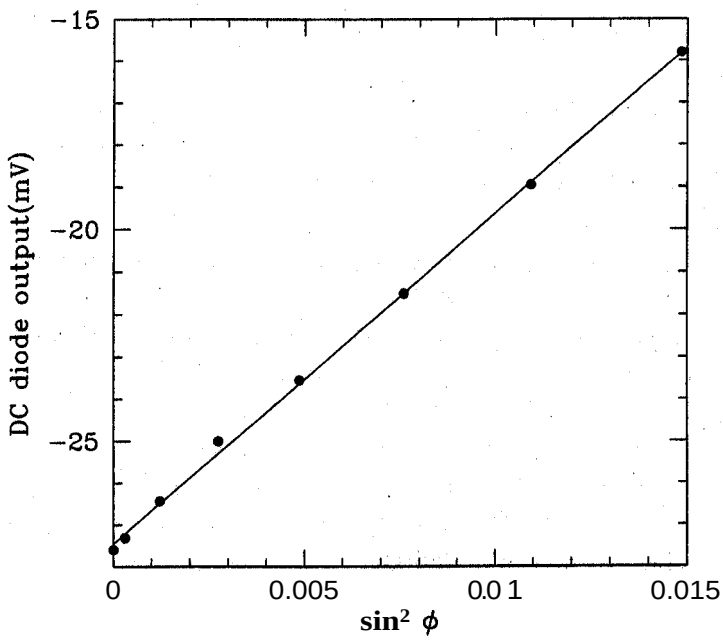

Figure 6.5: Variation of the transmitted light intensity (calculated from the data shown in Figure 6.4) as a function of $\sin^2\phi$. The straight line corresponds to the least squares fit used to calculate I_0.

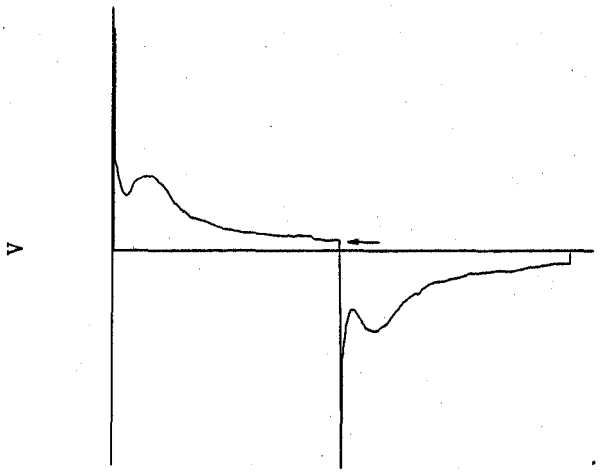

Figure 6.6: A typical trace of the voltage measured across R_m as seen on the oscilloscope when a large voltage is applied to the cell. The arrow indicates the position at which the current measurements have been made.

a function of time (as seen on the oscilloscope) when a large AC voltage ($\sim$ 250 volt) is applied to the cell. The first peak is due to the capacitive response of the cell as the voltage is switched from one polarity to the other. The second peak is due to the ionic current. When the voltage is small the second peak is almost absent. As the voltage is increased ions in the medium are swept towards the electrodes giving rise to the second peak. The ions collect near the electrodes and do not contribute to the conduction during the remaining part of the half cycle. As the voltage is increased the second peak moves closer to the first peak and in some cases they merge together. The current has been measured from the oscilloscope trace just before the polarity is switched (indicated by the arrow in Figure 6.6). For higher voltages the measured current is due to the residual ions.

The experiment is conducted by holding the sample at a specific temperature and applying the voltage which is increased in steps. These experiments were not computer controlled. The experiments were conducted at different temperatures as the sample was cooled. The local heating of the sample was not measured and the temperatures plotted in the diagrams to be presented are those of the Mettler hot stage.

Figures 6.7 and 6.8 show the variation of the 2f optical signal and the current in an 80CB sample as a function of field at 75°C. Figures 6.9 to 6.12 show the variation of the optical signal and the current in 5CT and ROCP7334 at different temperatures as a function of field. The frequency of the applied voltage was 256 Hz.

From Figures 6.7, 6.9 and 6.11 we see that the optical response starts to increase at a threshold field. It attains a peak at intermediate fields and as the field is further increased the optical response starts to decrease. In both 5CT and ROCP7334 the threshold for the optical response increases with decrease of temperature. In 5CT the width of the peak decreases with decrease of temperature and the peak position is insensitive to temperature and occurs at $\sim$ 250 esu. On the other hand in ROCP7334 the peak width increases with decrease of temperature and the peak position generally shifts to higher fields at lower temperatures (except between 130°C and 140°C).

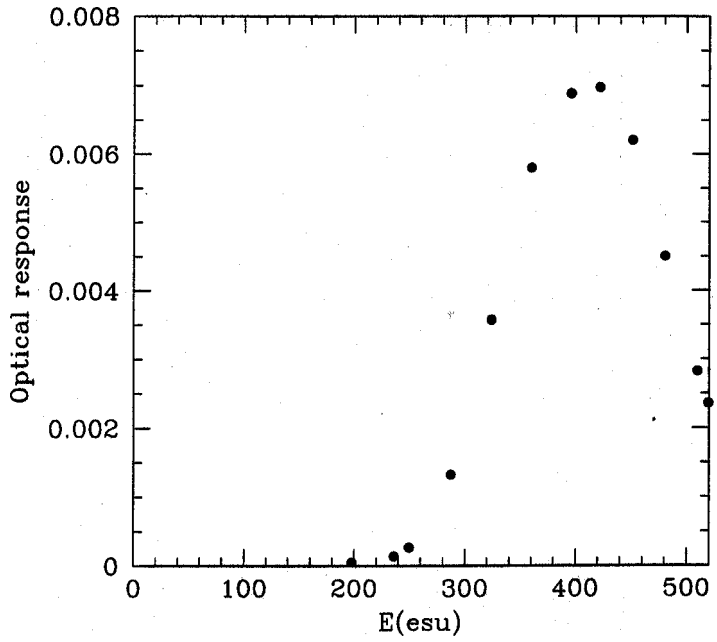

Figure 6.7: Variation of the 2f electrooptic response as a function of applied field of an 80CB sample d = 27 μm, T =75°C, f =256 Hz.

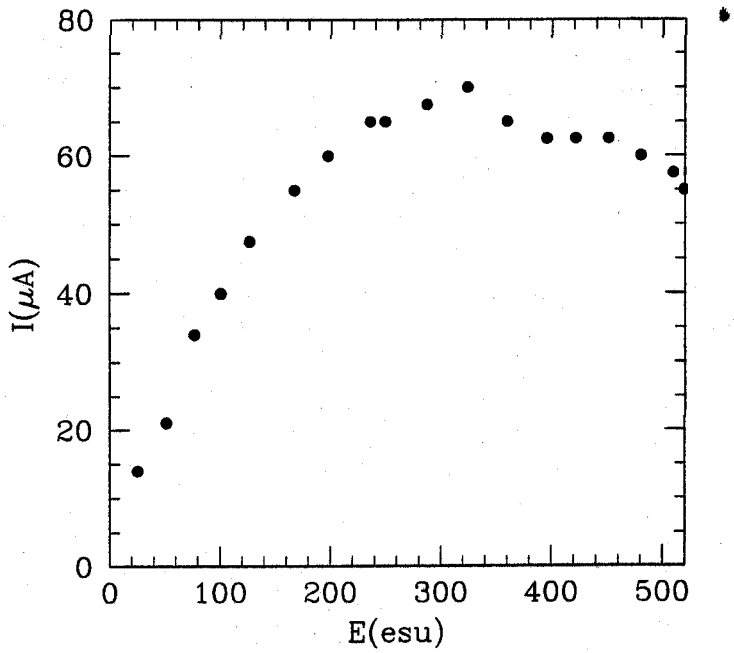

Figure 6.8: Variation of the current flowing through an 80CB sample as a function of field. Same sample as in Figure 6.7.

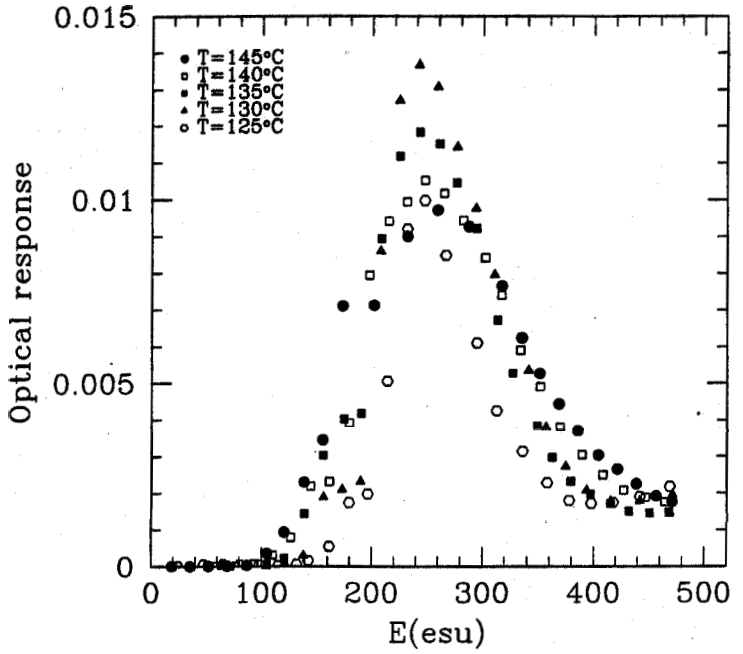

Figure 6.9: Variation of the *2f* electrooptic response as a function of applied field of a 5CT sample, d = *29* μm, at different temperatures (f=256 Hz).

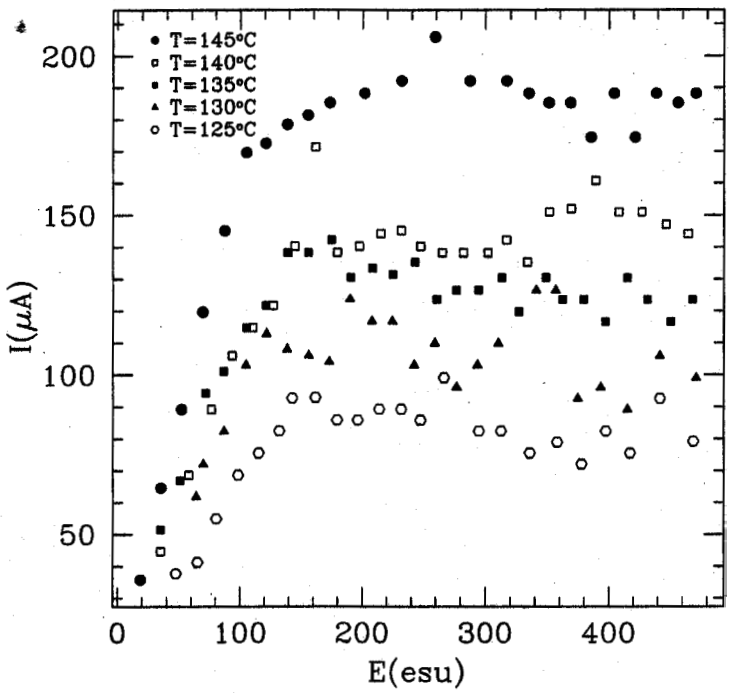

Figure 6.10: Variation of the current flowing through a 5CT sample as a function of field at different temperatures. Same sample as in Figure 6.9.

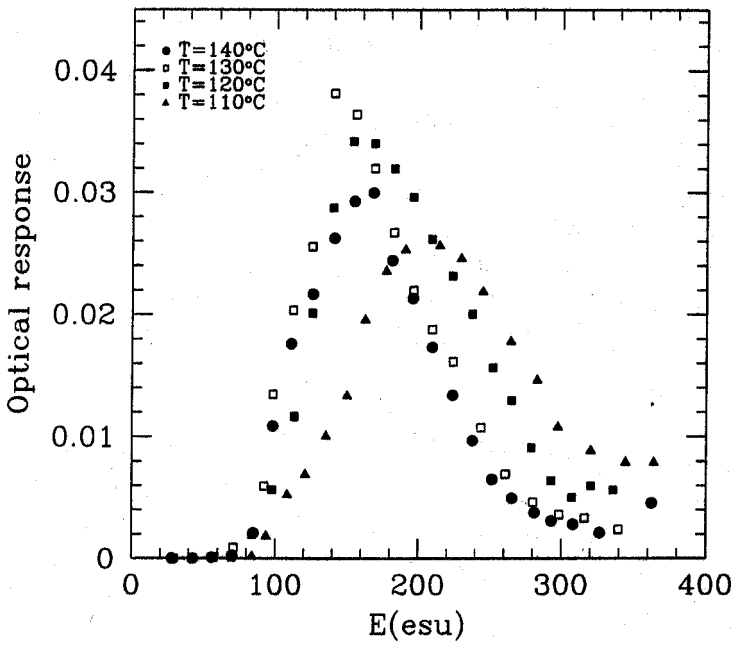

Figure 6.11: Variation of the 2f electrooptic response as a function of applied field at different temperatures for ROCP7334, d = 35.9 μm f=256 Hz.

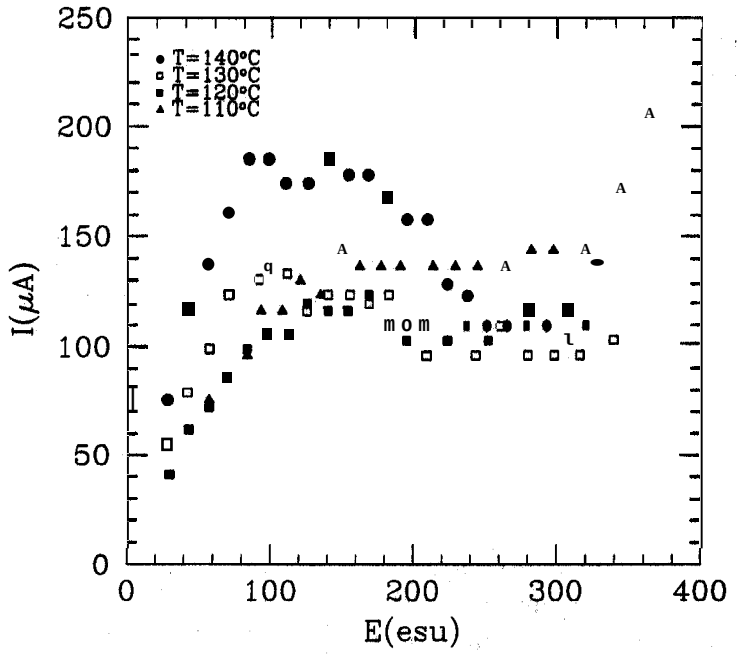

Figure 6.12: Variation of the current flowing through an ROCP7334 sample as a function of field at different temperatures. Same sample as in Figure 6.11.

From Figures 6.8, 6.10 and 6.12 we see that for low fields the current increases almost linearly with increase of field. At higher fields it grows less rapidly and beyond some field the current gets saturated (levels off). In 5CT for all the temperatures the current remains almost constant as the field is increased from ~ 100 to ~500 esu. In 8OCB initially the current saturates and then starts to decrease as the field is further increased. In ROCP7334 at 140°C the current saturates at ~100 esu and as the field is increased beyond 160 esu it starts to decrease. This trend is also seen at 130°C and 120°C whereas for the 110°C run the maximum in current is absent but at ~ 315 esu the current starts to increase again. In 5CT we see an almost systematic increase in the current as the temperature is increased, at all fields. This is true in ROCP7334 only for fields below 100 esu. As in the case of the electrooptic response the limiting current occurs at lower fields as the temperature is increased.

As shown in Figure 6.6 for higher voltages a second peak in the current is seen on the oscilloscope. This is due to the sweeping of the ions to the electrodes when the voltage is reversed. The voltage at which this second peak starts to form coincides with that at which the current starts to saturate. As mentioned the current measurement is made at the end of half the voltage period. For lower voltages apart from the initial peak due to the capacitive response the current is practically constant during the rest of the half cycle. We thus measure the average current. For higher voltages we measure the current due to the residual ions which may arise from a dissociation reaction in the bulk. The most important observation from these studies is that the threshold of the optical response occurs at the field where the current in the sample gets limited.

The conductivity has been calculated using the relationship

$$\sigma = \frac{d}{R_s A} \tag{6.2}$$

where R_s is the resistance of the sample. d and A are the thickness and the active area of the cell respectively. The conductivity measurements presented here are different from those presented in Chapters 4 and 5. In the latter, the measurements are made using a lock-in-amplifier and the conductivity is averaged over the voltage cycle. In the measurements described in this chapter

$$R_s = IV_A \tag{6.3}$$

where V_A is the applied voltage and I is the current measured across the series resistor just before the polarity of the voltage is reversed (ignoring the small voltage drop across the series resistor). We again point out that this current at higher voltages is due to the residual ions.

Figures 6.13, 6.14 and 6.15 show the variation of the conductivity in 8OCB, 5CT and ROCP7334 samples as'calculated from the data shown in Figures 6.8, 6.10 and 6.12 respectively. As these measurements were made by manually noting down the readings from the oscilloscope the inaccuracies in these conductivity measurements are larger than those presented in Chapters 4 and 5. In all the figures we can see that as the field is increased there is an overall decrease in the conductivity. In 5CT as the the temperature increases the conductivity increases. In ROCP7334 below 100 esu the conductivity increases with temperature. Above '100 esu the conductivity at llO°C starts to become larger than that at 120°C and 130°C. Above ~ 220 esu the conductivity at 110°C becomes even larger than the conductivity at 140°C. These observations are consistent with the resistance measurements described in Chapter 5. As discussed previously (Chapter 5) we attribute the decrease of conductivity as the field is increased to the electrolytic nature of the sample (see also Section 6.3.1). As the temperature is increased the conductivity goes up due to the greater mobility of ionic impurities along $\hat{n}$. At lower temperatures for high electric

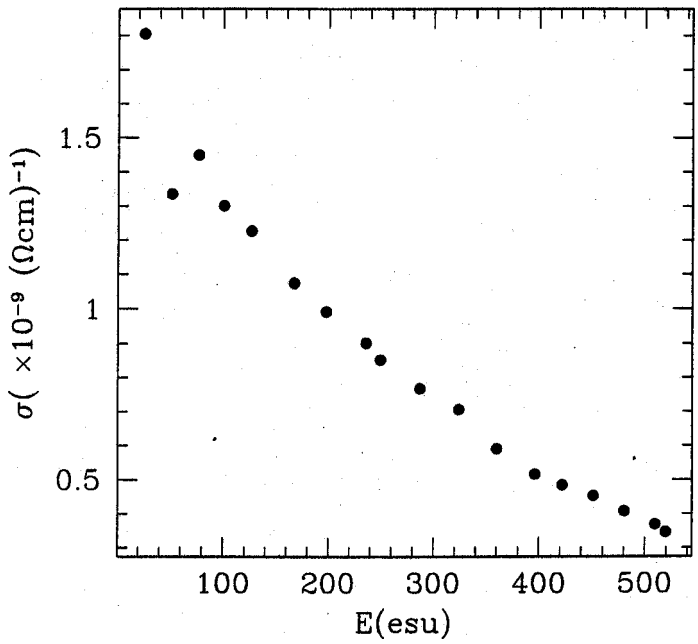

Figure 6.13: Variation of the conductivity of the 8OCB sample as a function of field. Calculated from the data shown in Figure 6.8.

fields the conductivity can increase due to the enhancement of the orientational order parameter in the medium. This process might explain the increase in conductivity in ROCP7334 at lower temperatures when the field is large.

We have also measured the optical response in ROCP7334 as a function of field at different frequencies (Figure 6.16). It can be seen that the electrooptic response has a threshold at higher fields for higher frequencies and also the height of the peak decreases with increase of frequency. In 5CT we have measured the optical response as a function of frequency at different temperatures keeping the applied voltage constant (V=275 V, Figure 6.17). It can seen that at all the temperatures the optical response shows a quasi resonance (i.e. a peak at a certain frequency). There is an overall increase of the frequency at which the optical response shows a peak as the temperature is increased.

Visual observations in the microscope show that there is an erratic motion of dust particles for fields $\geq$ 100 esu. We do not see the formation of electrohydrodynamic instabilities in the fresh samples which were used in the measurements reported in Figures 6.7 to 6.17. However we do see a brightening and a subsequent darkening of the field of view as the electric field is increased in the voltage range in which the electrooptic response is measured. This is reflected in the DC optical response of an ROCP7334 sample as a function of field at different temperatures as shown in Figure 6.18. The DC intensity profile is indeed very similar to the AC intensity profile shown in Figure 6.11. After the cells were exposed to low frequency high fields for a long time ($\sim$ 1 week) in some of the cells we did see the formation of electrohydrodynamic instabilities and also the formation of maltese crosses as reported in previous experiments [29, 89].

The different mechanisms which can give rise to electrooptic effects in liquid crystals arise from dielectric, surface polarisation, flexoelectric and electrohydrodynamic effects [1, 2, 29, 90]. In the homeotropic geometry the director is along the direction of the field and the dielectric anisotropy favours the undistorted state. We used a square wave excitation so that E^2 is constant

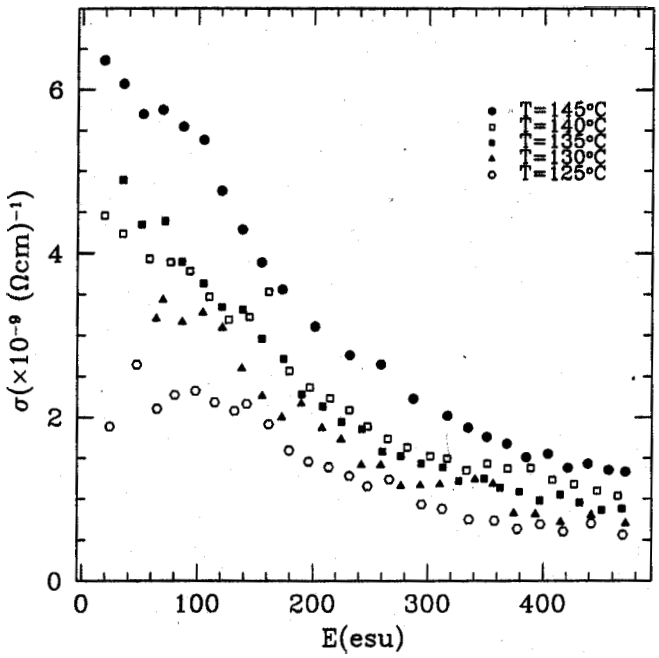

Figure 6.14: Variation of the conductivity of the 5CT sample as a function of field at different temperatures. Calculated from the data shown in Figure 6.10.

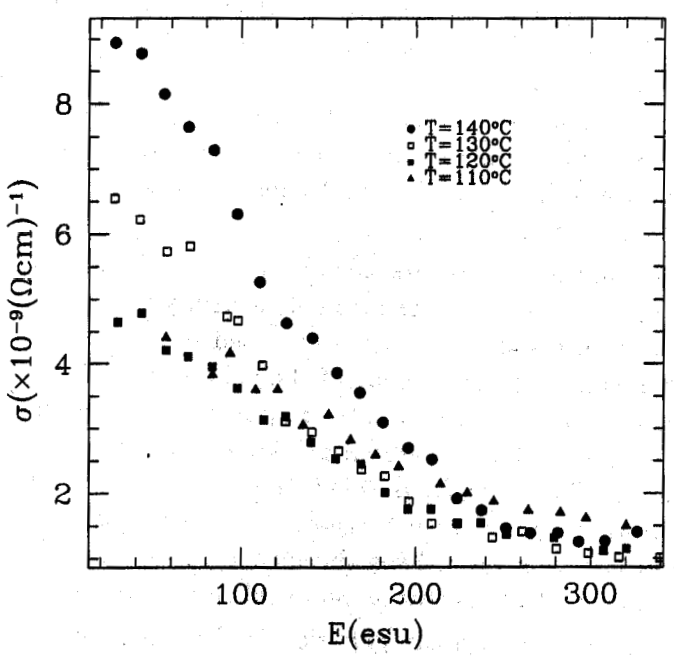

Figure 6.15: Variation of the conductivity of ROCP7334 as a function of field at different temperatures. Calculated from the data shown in Figure 6.12

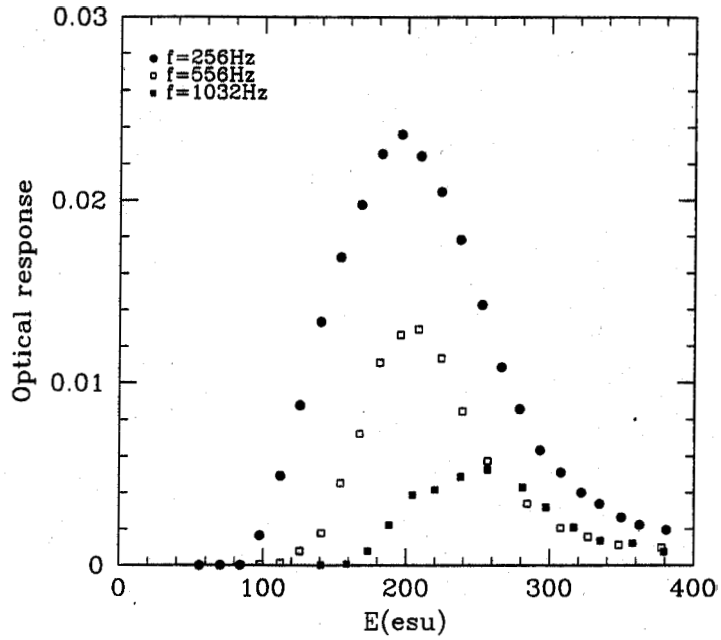

Figure 6.16: Variation of the 2f optical response of an ROCP7334 sample as a function of field at different frequencies. Same sample as shown in Figure 6.11, T=130°C.

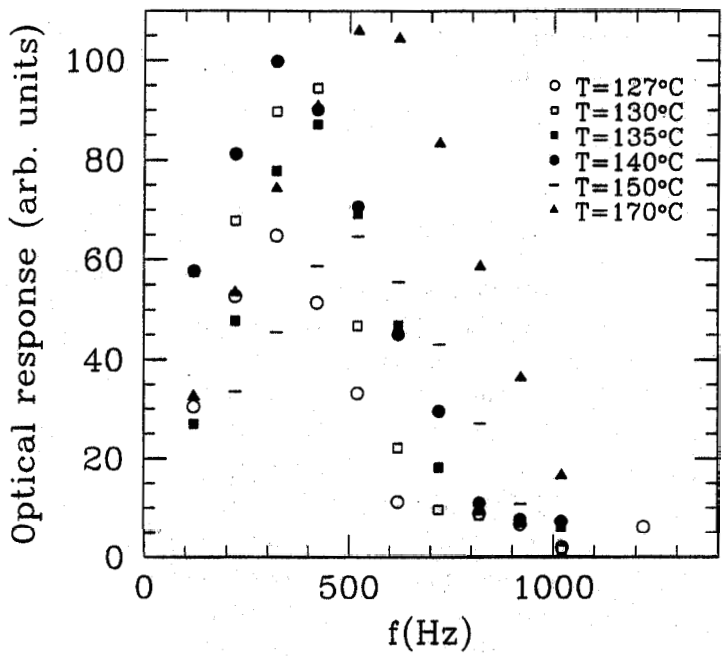

Figure 6.17: Variation of the 2f optical response of 5CT sample as a function of frequency at different temperatures. V=275 V and d = 29 μm.

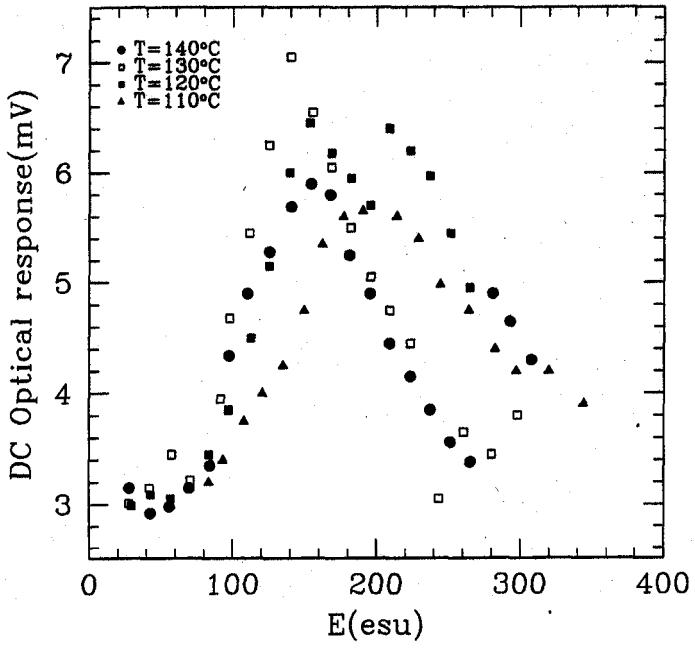

Figure 6.18: Variation of the DC optical response in ROCP7334 as a function of field at different temperatures. Same sample as shown in Figure 6.11.

and any response due to quenching of thermal fluctuations of the director (described in Chapter 5) is time independent. The possibility of a deformation in the director field due to surface polarisation has been discussed and experimentally demonstrated by Durand et *al* [90, 91, 92]. In the next section we describe experimental results which show that at low fields the surface polarisation effect does produce an electrooptic effect. However at the higher fields at which we have seen the peak in the electrooptic response the latter cannot be attributed to a distortion caused by surface polarisation.

6.2.2 Electrooptic Response due to Surface Polarisation

The polar symmetry of any nematic-solid interface allows in principle the existence of a surface ferroelectric nematic order. Figure 6.19a shows the schematic diagram of the surface orientation of polar molecules when the nematic liquid crystal is taken between two glass plates coated for homeotropic alignment. The arrows show the direction of the surface polaxisation (the actual direction for the polarisatian, $\vec{P}_s$, depends on the surface treatment and the type of molecules in the liquid crystal). In the absence of a field in this geometry there is no flexoelectric polarisation. In the presence of an electric field $\vec{P}_s$ tends to align along the direction of the field. It can be seen from Figure 6.19b that for one of the surfaces of the cell this condition is already satisfied. For the other surface this is not so, and hence the coupling of this surface polarisation with the electric field gives rise to an instability at a threshold field (i.e. when the surface energy equals the coupling energy of the field with the surface polarisation).

As discussed in Section 6.2.1 we have observed a peak in the electroogtic response when the applied low frequency field is relatively large. In order to check if this response can arise from the surface polarisation we conducted an experiment on 5CT following the procedure described by Lavrentovich et *al* [91].

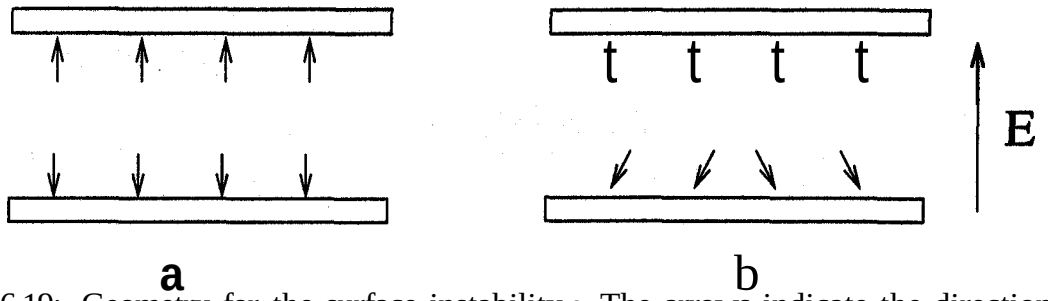

Figure 6.19: Geometry for the surface instability : The arrows indicate the direction of the surface polarisation due to the polarity of the molecules. (a) In the absence of voltage (b) Above the surface instability threshold. The splay in the polarisation indicates an inhomogeneity of the director near the lower surface.

A DC electric field produces the instability near the electrode$ at one of the surfaces at a threshold field due to the surface polarisation (Figure 6.19). On the other hand a high frequency AC electric field tends to align the director parallel to the electric field as 5CT has a strong positive dielectric anisotropy. When simultaneously a high frequency AC and DC electric fields are applied to the cell, the AC field restabilises the surface alignment of the director. Thus in the presence of a high frequency AC field the threshold field for the surface instability has a higher value.

We have undertaken this study on a 27 μm thick 5CT sample maintained at 130°C. The schematic diagram of the experimental setup is shown in Figure 6.20. The DC and sinusoidal AC voltages were applied from the HP synthesizer without amplification. We have used white light to illuminate the sample. The Mettler photomonitor attached to the microscope has been used to detect the threshold for the instability. This threshold was characterised by a large increase of the light intensity as measured by the photomonitor.

At a set frequency the AC voltage is increased in steps and for each set AC voltage, the DC threshold voltage is determined. Visual observations of the samples show cloudy patterns, which are similar to those reported by Monkade et *al* [90]. Figure 6.21 shows the DC threshold voltage (U_{DC}) for the instability as a function of applied AC voltage (U_{AC}) at different frequencies. There is an uncertainty of the DC threshold voltage of $\sim \pm 0.2$ V in the absence of the AC voltage. From Figure 6.21, it is seen that at any given AC voltage as the frequency is increased up to 10 kHz generally the DC threshold voltage increases. At 20 kHz the DC threshold voltage decreases compared to that at 10 kHz.

At 1 kHz and 5 kHz the DC threshold voltage initially decreases as the AC voltage is increased (till $U_{AC} \sim 4.0$ V) and then it starts to increase. At all the frequencies there is a change of slope in U_{DC} as a function of U_{AC} at $U_{AC} \sim 4.0$ V. Beyond $U_{AC} = 4.0$ V, U_{DC} varies linearly with U_{AC}. Drawing straight lines through the experimental data for $U_{AC} > 4.0$ V and extrapolating them to $U_{AC}=0$ it is seen that all the lines converge to $U_{DC} \simeq 2.0$ V. This is ~ 0.6 V below the actual U_{DC} in the absence of a stabilising AC voltage.

As was shown by Lavrentovich et *al* [91], for an insulating medium the DC threshold field ($E_{DC,Th}$) when an AC field is applied simultaneously is given by

$$E_{DC,Th} = \frac{K}{e^* - \left(\frac{\epsilon_a K}{4\pi}\right)^{\frac{1}{2}}} \left[\frac{|E_{AC}|}{\left(\frac{4\pi K}{\epsilon_a}\right)^{\frac{1}{2}}} + \frac{1}{L} \right] \tag{6.4}$$

where K is the elastic constant, in the one constant approximation, e^* is the sum of the flexo-

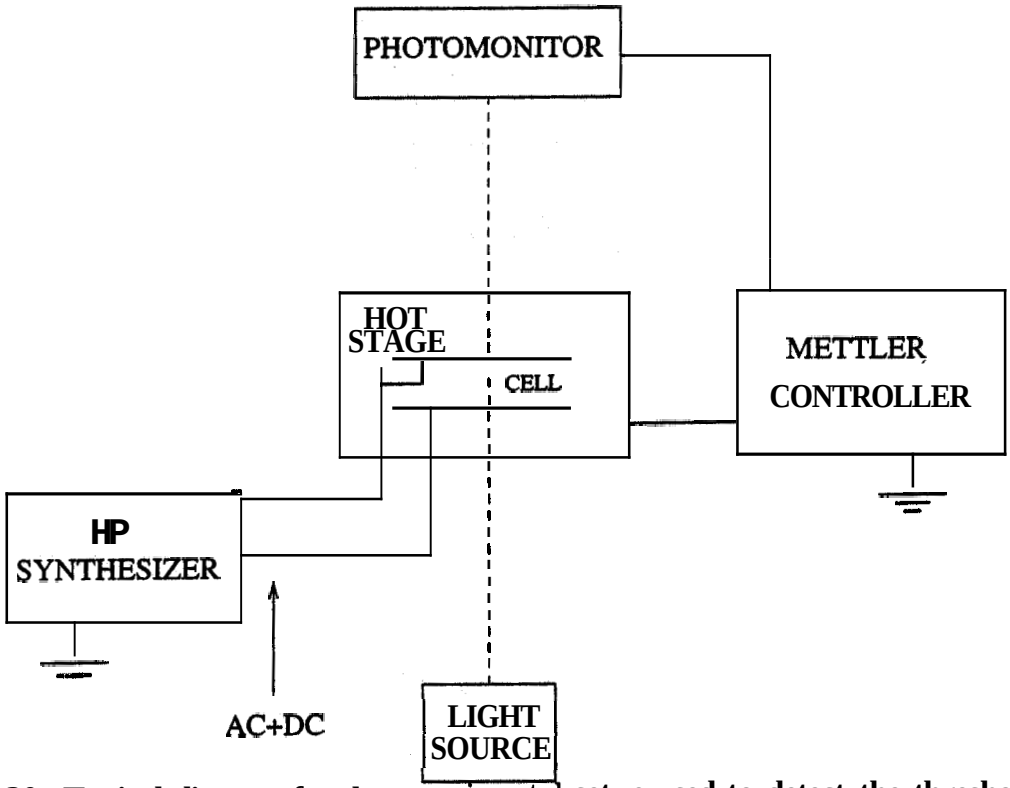

Figure 6.20: Typical diagram for the experimental setup used to detect the threshold of the surface instability.

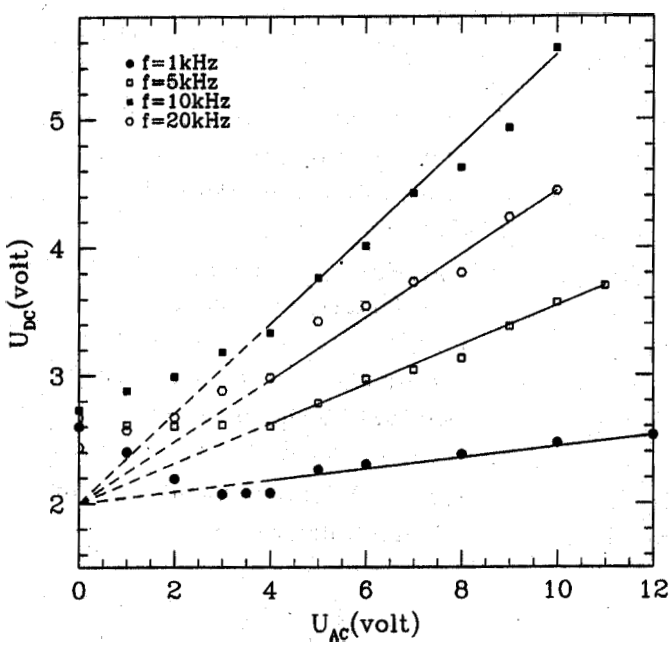

Figure 6.21: The DC voltage threshold, U_{DC} of the surface polar instability as a function of applied AC field at different frequencies, d=27 μm.

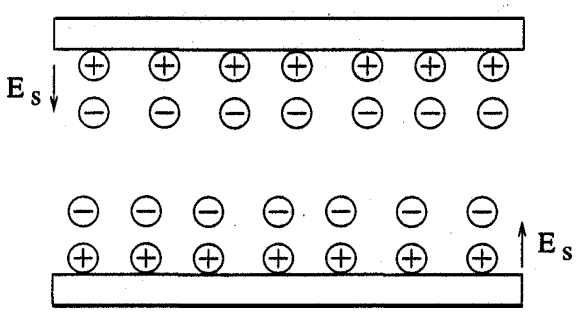

Figure 6.22: Schematic diagram showing the formation of the surface field (E,) near the electrodes due to adsorbed ions. We have assumed that the positive ions get adsorbed to the surface of the cell.

electric and surface polarisations, E_{AC} is the applied AC electric field and L is the extrapolation length characterising the inverse strength of the surface anchoring [1]. According to Equation 6.4 the instability occurs at a higher DC threshold field when an AC electric field is simultaneously applied. In the experimental results reported by Lavrentovich et *al* [91] on 5CB the DC threshold voltage was seen to be independent of frequency of the AC voltage. On the other hand in our experiments on 5CT the DC threshold voltage depends on the frequency of the AC voltage.

It should be noted that the measurements on 5CT are made at a much higher temperature (130°C) than those on 5CB (20°C). Thus due to the higher sample temperature 5CT can be expected to have a larger conductivity than 5CB. From Figure 6.14 we can see that the conductivity of the 5CT sample is $\sim 4\times10^{-9}(\Omega\text{cm})^{-1}$. We attribute the frequency dependence of U_{DC} in the presence of an AC field to be due to large ionic conductivity of the sample.

As explained above when we linearly extrapolate the lines through the data points beyond $U_{AC} = 4.0\ V$ to $U_{AC} = 0$ we see that they converge to U_{DC} =2.0 V. This is $\sim$ 0.6 V less than the experimentally observed DC threshold voltage in the absence of an AC voltage. This implies that in the absence of an external field there is a potential at the surface corresponding to $\sim$ 0.6 V. This potential stabilises the surface alignment hence increasing the DC threshold voltage for the surface deformation. It is known that depending on the nature of the surface and the ionic impurities either positive or negative ions get adsorbed on the surface [93]. Due to the adsorbed ions an ion cloud of opposite charges will get attracted to the surface (Figure 6.22). We have assumed that positive ions get adsorbed by the electrodes and the negative counter ions form the ion cloud. This produces a surface field (E,) localised over a distance L_D called the Debye screening length. The ion charge densities (ρ_+ and p,) and the potential in the cell due to adsorbed charges have been calculated by Barbero and Durand [93]. A typical variation of the quantities are shown in Figure 6.23 as a function of distance from the electrodes.

It is seen in the experimental data (Figure 6.21) that for low frequency AC voltages (1 kHz and 5 kHz) U_{DC} initially decreases as U_{AC} is increased up to 4.0 V. This implies that the ion cloud at the surface is deformed due to the AC field thus bringing down E_s which in turn brings down U_{DC}. This effect is obviously larger than the stabilisation of the alignment due to the AC field up to 4.0 V. For higher frequencies we see that U_{DC} increases with increase of U_{AC} right from the beginning implying that the effect on the double layer by the AC field is much smaller than at lower frequencies as the dielectric stabilisation produces a positive slope. At U_{AC}=4.0 V we see a change in slope in U_{DC} as a function of U_{AC} for all the frequencies. Beyond U_{AC}=4.0

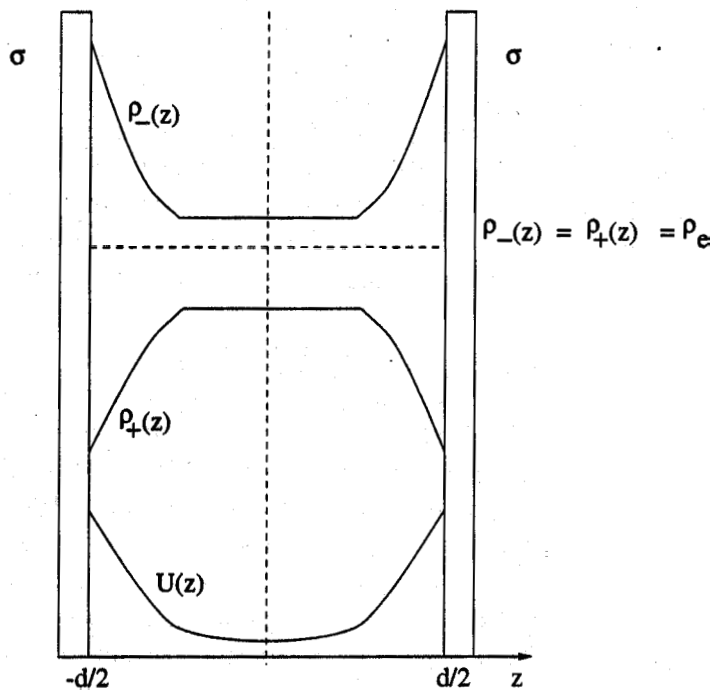

Figure **6.23:** Schematic diagram of the dependence of the potential U and the ion charge densities ρ_+ and ρ_- on the distance from the electrodes. The plates are assumed to adsorb positive ions of surface density σ. ρ_e is the equilibrium concentration of the neutral solution in the absence of adsorption. The electric field is localised near close to the plate at $\pm d/2$ over a Debye screening length. Adapted from Reference [93].

V, U_{DC} depends linearly on U_{AC} as expected from the functional form shown in Equation 6.4. It appears that beyond an AC voltage of 4.0 V the counter ion cloud is no longer effective thus reducing E_s.

For a conducting medium under the action of a field, the total current density ($\vec{J}$) is a constant [94]:

$$\vec{J} = \sigma\vec{E} + \frac{\partial\vec{D}}{\partial t} \tag{6.5}$$

where $\vec{D}$ is the displacement vector. From the experiment described above we see that a has both a spatial and time dependence. This leads to a spatially and temporally dependent local field [94]. A quantitative understanding requires a detailed theoretical analysis which takes into account the adsorption of ions, the time and spatial dependences of the ionic conductivity which depends on the ion density profile and the local field in the sample cell. Such an analysis is beyond the scope of this thesis.

Even in measurements above 4.0 V we see that the DC threshold voltage depends on the frequency of the applied AC voltage. As described in Chapters 4 and 5 the conductivity (a) of the sample has contributions from both the ionic conductivity and from the relaxation of $\epsilon_{\|}$. As the frequency is increased the contribution from the relaxation of $\epsilon_{\|}$ increases. This may explain the initial increase of U_{DC} as the frequency is increased up to 10 kHz and also the subsequent decrease at 20 kHz.

6.3 Discussion

From the measurements on the surface instability we can see that it gets suppressed for very low AC voltages i.e. even in the presence of a low AC voltage a DC field is required to form the surface instability. Higher AC voltages only stabilise the alignment due to the dielectric coupling. In the experiments described in Section 6.2.1 the peak in the optical response is observed at much higher AC fields than those used in the experiments on the surface instability described in Section 6.2.2. Thus we cannot attribute the peak in the electrooptic response to be due to the formation of a surface instability.

6.3.1 Electrolytic Nature of Liquid Crystals:Limiting Current

Due to the presence of ionic impurities, liquid crystals behave as weak electrolytic solutions [29, 79, 95, 96, 97]. The conductivity of the liquid crystal can mainly be attributed to two different mechanisms [79]. In low DC fields the electrical behaviour is due to thermal dissociation of the ionic impurities in the sample. At higher DC fields charges get injected from the electrodes. The latter process may not be important in our experiments as we have used AC fields [29].

In equilibrium we can assume that the impurity is like a weak electrolyte giving rise to the following dissociation reaction:

$$AB \underset{K_R}{\overset{K_D}{\rightleftharpoons}} A^+ + B^-$$

where AB is the concentration of nondissociated species and A^+ and B^- are the dissociated ion concentrations. K_D and K_R are the dissociation and recombination constants for the reaction. In the absence of any external field the conductivity of the sample is decided by the natural equilibrium of the dissociation reaction described above. On application of an electric field this equilibrium is disturbed owing to electrolysis. When the electric field is low the electrolysis rate is slow and the equilibrium is only slightly disturbed. Then the ionic conductivity of the sample

is only slightly different from the value it has in the absence of the field. In the presence of a high electric field the electrolysis rate increases and the ions formed due to the dissociation get swept towards the electrodes. This leads to a reduction of the ions available for conduction in the bulk. For higher fields the conductivity hence becomes independent of the applied field and attains a saturation i.e. the current gets limited. In the presence of an AC field, the field at which the current gets limited depends on the frequency of the applied AC voltage as the ions collected near one electrode should move to the other after the reversal of the field. If the frequency is higher the limiting current will occur at higher electric fields. The limiting of the current shown in Figures 6.8 6.10 and 6.12, correspond to 256 Hz. As mentioned for higher fields the current measurement is made at a time well after the occurrence of the current peak which arises due to the sweeping away of the ions (Figure 6.6) i.e. we measure the current due to residual ion impurities.

6.3.2 Electrohydrodynamic Instability in Materials with Positive Dielectric Anisotropy

There has been quite a body of work on the formation of electrohydrodynamic(EHD) instabilities in homeotropically aligned materials with positive dielectric anisotropy [29,98-104]. In all these studies the threshold for the onset of the EHD instability as a function of AC frequency and also of conductivity are measured. Sussman [104] has also seen EHD instability patterns which modulate at twice the frequency of the applied voltage.

In the experiments conducted by Trufanov *et al* [99] as the voltage is increased they initially observe liquid flow (detected by dust particle motion) and when the voltage is further increased they observe an EHD instability pattern in the form of maltese crosses throughout the sample.

An *isotropic mechanism* has been proposed to explain the occurrence of this instability [29]. According to this mechanism the instability is caused by a nonuniform distribution of the space charge in the sample which is concentrated near one of the electrodes as a result of either unipolar injection or due to the collection of charges on the application of an external field. According to this model all the electrostatic energy is converted into kinetic energy making the ions to drift towards the electrodes along with the flow of the liquid. This gives rise to a convective flow which is similar to that seen in isotropic liquids exposed to a temperature gradient. Figure 6.24 shows the geometry for the formation of the instability due to the isotropic mechanism.

Pikin [89, 30] has suggested that under the application of an AC field the distribution of charges (Q) along the layer thickness should obey the following dependence on the electric field:

$$\frac{\partial Q}{\partial z} = -\nu E \tag{6.6}$$

where ν is a kinetic coefficient. According to their model for frequencies less than the charge relaxation frequency ($\tau_c = \frac{4\pi\sigma}{\epsilon}$) the threshold field ($E_{th}$) for a convective instability is given by

$$E_{th}^2 = \frac{128\pi^4\eta\sigma}{\epsilon^2} \tag{6.7}$$

where $\eta = \alpha_4/2$ and α_4 is a viscosity coefficient. Using typical values for $\sigma(\simeq 10^{-9}$ (ohm cm)$^{-1})$ and $\epsilon(\simeq 10)$ and $\alpha_4/2(\simeq 30$ cP for 5CB [30]) $\tau_c \simeq 1000$ Hz. In our experiments f = 256 Hz which is less than the charge relaxation frequency. Hence from Equation 6.7 $E_{th} \sim 60$ esu. This is about half the value at which we see the onset of the optical response (for 5CT). From this theory only the threshold for the onset of the convective instability has been estimated.

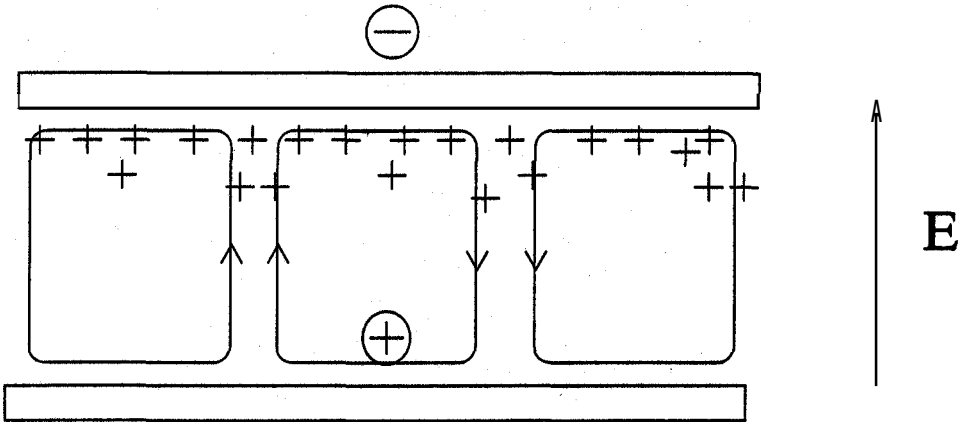

Figure 6.24: An electrohydrodynamic instability when there is charge collection near one of the electrodes. The arrows indicate the direction of the flow of the liquid.

In our experiments as mentioned previously we do not see the formation of maltese crosses for fresh samples in which the measurements of the optical response are made. Also the particle motion seems to be erratic rather than circular in nature. Hence, we do not believe that it arises from the EHD instability. But the fact that the optical response occurs beyond the field at which the current is *limited* implies that the electrolytic nature of the sample is important for the origin of the electrooptic response. In the next section we present an alternative mechanism to get an electrooptic response in a nematic liquid crystal sample due the presence of a strong field gradient near the electrodes.

6.3.3 Possible Origin of the Formation of an Optical Response due to the Coupling of Flexoelectric Polarisation with a Field Gradient

As described earlier, the current measurements reported in Section 6.2.1, show that for high fields the ions are swept towards the electrodes. This causes a nonuniformity of the charge distribution in the sample near the electrodes and in turn produces a field gradient (see Figure 6.26). Due to the ions getting concentrated near the electrodes the field gradient can be very large near the electrodes. This large field gradient can couple with the ***flexoelectric polarisation*** which leads to another mechanism which can produce an instability.

A macroscopic polarisation can be induced in a nematic liquid crystal by splay and bend distortions of the director field. This flexoelectric polarisation was first shown by Meyer to be of the form [88],

$$\vec{P_f} = e_1\hat{n}(\nabla \cdot 6) + e_3(\nabla \times 6) \times \hat{n} \tag{6.8}$$

where e_1 and e_3 are the flexoelectric coefficientscorresponding to the splay and bend deformations of the director field respectively.

As the response due to the flexoelectric polarisation has to compete with the stabilizing dielectric response in the presence of a strong electric field, we compare the torques on the director due to the flexoelectric and dielectric responses respectively. For this purpose we calculate the molecular field (h_i) using which the torque can be calculated. The molecular field is given by

$$h_i = -\frac{\partial F}{\partial n_i} + \partial_j \frac{\partial F}{\partial g_{ij}} = -C(\vec{r})n_i \tag{6.9}$$

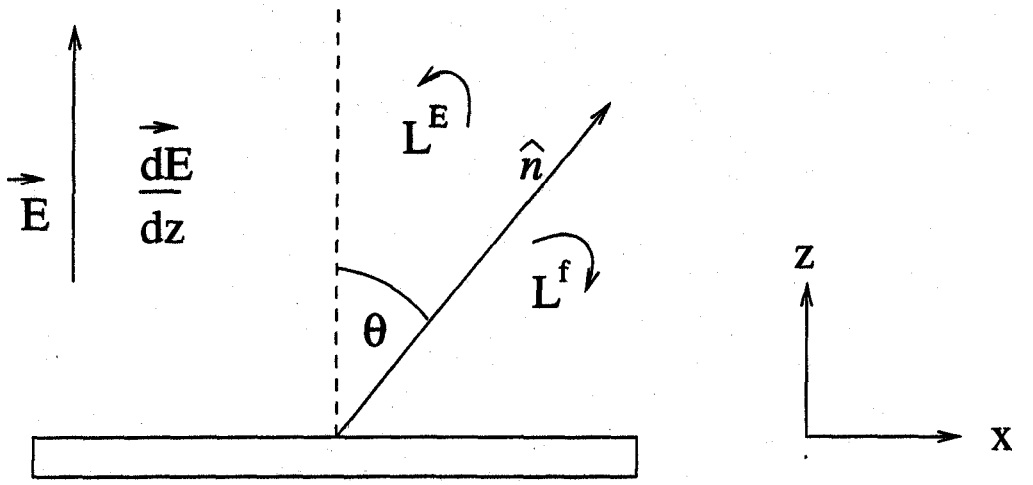

Figure 6.25: Schematic diagram of the deviation of the director form the field direction due to the coupling of the flexoelectric polarisation with the field gradient.

where F is the free energy density, $\partial_j = \frac{\partial}{\partial x_j}$, $g_{ij} = \partial_j n_i$, and $C(\vec{r})$ is an arbitrary function of $\vec{r}$. At equilibrium the director $(\hat{n})$ should be parallel to the molecular field. When A and $\vec{h}$ are not parallel then the director experiences a torque which is given by $\hat{n} \times \vec{h}$.

The orientational part of the dielectric free energy density is given by

$$F^E = -\frac{\epsilon_a}{8\pi}(\hat{n} \cdot \vec{E})^2. \tag{6.10}$$

We assume that the director is confined to the x-z plane and the electric field is along the z direction (see Figure 6.25). The components of the director are then

$$\mathrm{A} = (\sin\theta, 0, \cos 8) \tag{6.11}$$

where θ is measured with respect to the normal to the glass plate. The free energy density due to the flexoelectric polarisation (F^f) is given by $-P$. E. Equations 6.11 and 6.8 lead to

$$F^f = \frac{(e_1 + e_3)}{2} \sin 2\theta \frac{\partial \theta}{\partial z} E \tag{6.12}$$

Using Equation 6.9 we calculate the bulk torques due to flexoelectricity (L^f) and the dielectric anisotropy (L^E) to be

$$L^f = \frac{(e_1 + e_3)}{2} \sin 2\theta \frac{\partial E}{\partial z} \tag{6.13}$$

and

$$L^E = \frac{\epsilon_a E^2}{8\pi} \sin 28. \tag{6.14}$$

In our experimental geometry the dielectric torque favours the director to be along the direction of the electric field. Thus for the flexoelectric torque to produce a deformation of the director away from the field direction it should be opposite to the dielectric torque. $(e_1 + e_3)$ has been measured for 80CB and ROCP7334 and it is found to be positive in both cases [105]. Thus from the above argument we can see that in these cases the field gradient should be negative. This is possible if we have a collection of negative charges near the positive electrode as shown in Figure 6.26. We have ignored the surface anchoring energy assuming that it is very small at

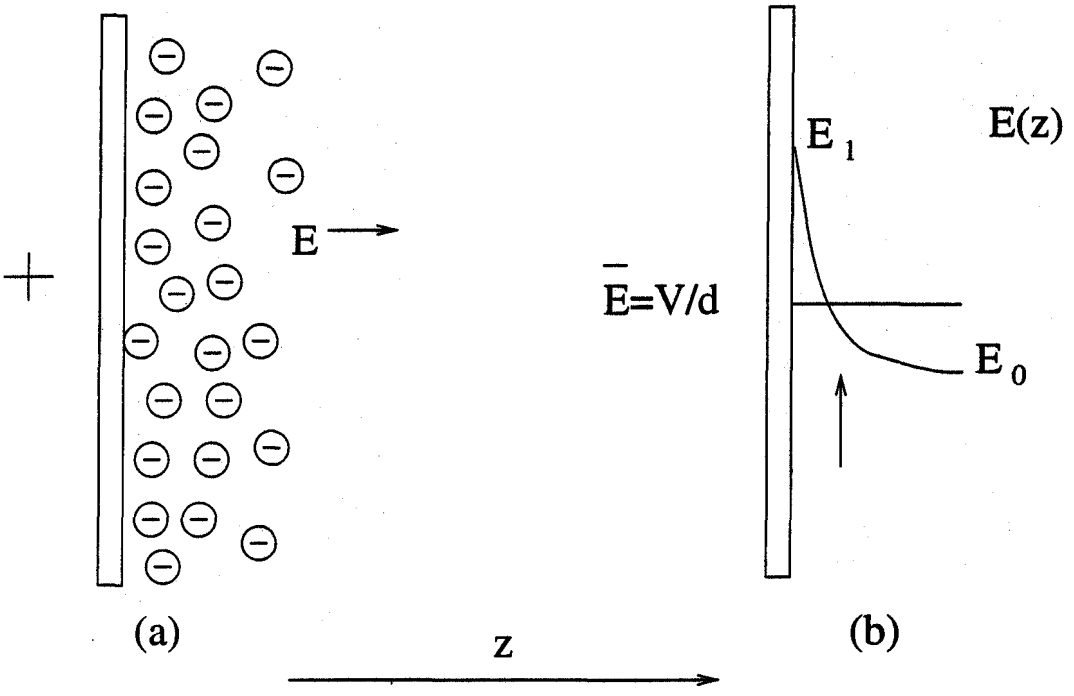

Figure 6.26: Schematic diagram of the charge distribution (a) and the field (b) near the electrodes when a large external voltage is applied to the cell. The horizontal line corresponds to the average field E. E_1 and E_0 are the values of the electric field near the electrode and in the bulk respectively.

the relatively high temperatures of measurement. Ignoring the elastic torque and equating the dielectric torque to the flexoelectric torque, we estimate the threshold field gradient required to produce an instability as

$$\frac{dE}{dz} = \frac{\epsilon_a E^2}{4\pi(e_1 + e_3)}. \tag{6.15}$$

For very high electric fields the alignment will be restabilised due to the strong dielectric torque. Thus as a function of field the optical transmitted intensity will initially show an increase when the instability sets in, and then as the field is increased further, shows a decrease as the alignment is restabilised. This can explain the optical peak observed in Figures 6.7, 6.9, 6.11.

Using typical values for E (2: 100 esu) at which the optical response is just visible and $(e_1 + e_3)(\simeq 10^{-3}$ cgs units) from Equation 6.15 the calculated threshold field gradient $dE/dz \sim 10^7$ esu/cm. From Figure 6.26, the instability occurs in the position shown by the arrow where dE/dz becomes large. If the field increases from the bulk value, $E_o = 100$ esu to $E_1 = 200$ esu at the surface over a length of 0.1 μm, we get the required field gradient. The coherence length (ξ) gives a measure of the length over which the instability, produced at the position indicated by the arrow in Figure 6.26, penetrates the sample and is given by [1]

$$\xi = \left(\frac{K}{\frac{\epsilon_a}{4\pi}}\right)^{\frac{1}{2}} \frac{1}{|E|}. \tag{6.16}$$

Using typical values for ϵ_a (2: 10) and K ($\simeq 10^{-6}$ dynes) and assuming that E $\simeq$ 100 esu (corresponding to the threshold field for the optical response in 5CT) is constant throughout

the sample $\xi \sim 0.1\mu m$.

To calculate the transmitted optical intensity in the presence of an instability caused by the coupling of flexoelectric polarisation with the field gradient over a length ξ we initially calculate the optical path difference over the length ξ over which the deformation penetrates the sample. If n_o is the ordinary refractive index of the nematic liquid crystal, the path difference (Al) is given by

$$\Delta l = \int_0^{\xi} (n_{eff}(z) - n_o) dz \tag{6.17}$$

where $n_{eff}(z)$ is the effective refractive index. $n_{eff}(z)$ depends on $\theta(z)$ and is given by

$$\frac{1}{n_{eff}^2} = \frac{\cos^2\theta(z)}{n_o^2} + \frac{\sin^2\theta(z)}{n_e^2} \tag{6.18}$$

where n_o and n_e are the principal refractive indices of the medium. Substituting Equation 6.18 in Equation 6.17 we get

$$\Delta l = n_o \int_0^{\xi} \left(\frac{1}{1 - (\frac{n_e^2 - n_o^2}{n_e^2})^{\frac{1}{2}} \sin^2\theta} - 1 \right) dz. \tag{6.19}$$

The optical phase difference $\Delta\phi$ is given by

$$\Delta\phi = \frac{2\pi}{\lambda} \Delta l \tag{6.20}$$

where λ $(=0.633\mu m)$ is the wavelength of the light used in the experiments (Figure 6.9). Then the transmitted intensity (T) is given by

$$\begin{aligned} T &= <\sin^2 2\psi> \frac{1 - \cos\Delta\phi}{2} \\ &- \frac{1 - \cos\Delta\phi}{4} \end{aligned} \tag{6.21}$$

where ψ is the angle made by the plane containing the field direction and the deformed director with respect to the crossed polariser position. The averaging <> is due to the fact that the deformation can take place with an equal probability at any azimuthal angle ψ.

Using typical values for n_o $(=1.5)$ and n_e $(=1.65)$ and assuming a deviation of the director from the normal corresponding to the maximum flexoelectric and dielectric torques (i.e. $0 = 45°$) when the intensity maximum is observed, the transmitted intensity $T \sim 0.01$. This number is similar to the maximum optical intensity measured in our experiments.

A detailed theoretical analysis of this problem involves taking into account the time and spatial dependences of the conductivity and local field in the sample as well as the hydrodynamic torque, which is beyond the scope of this thesis. A greater understanding of the experimental results in this chapter require further experimental and theoretical studies. We can however note that the process discussed is unlikely to be important at frequencies of several kHz and hence in the experiments discussed in earlier chapters.

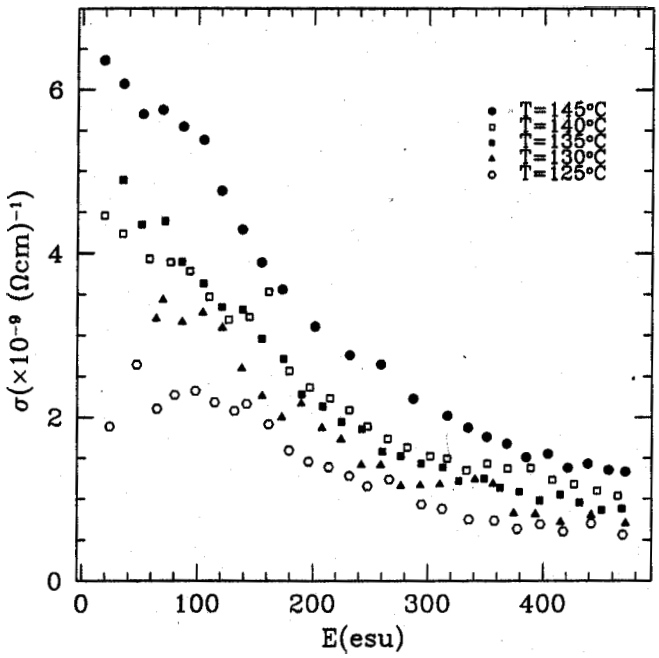

Figure 6.14: Variation of the conductivity of the 5CT sample as a function of field at different temperatures. Calculated from the data shown in Figure 6.10.

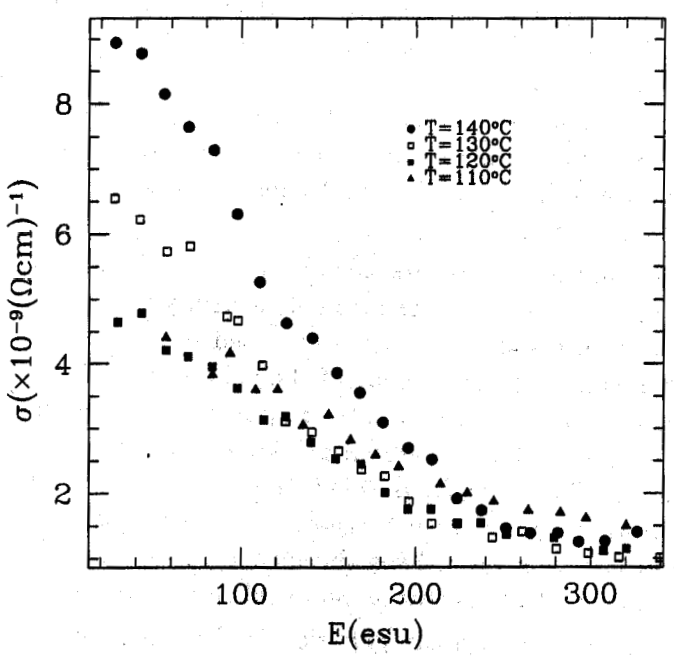

Figure 6.15: Variation of the conductivity of ROCP7334 as a function of field at different temperatures. Calculated from the data shown in Figure 6.12